



# Experimental visualization of sphere-induced oblique detonation in a non-uniform mixture

Kazuya Iwata <sup>a,\*</sup>, Naoki Hanyu <sup>b</sup>, Shinichi Maeda <sup>b</sup>, Tetsuro Obara <sup>b</sup>

<sup>a</sup> Graduate School of Science, Kyoto University, Kitashirakawa-Oiwake-cho, Sakyo-ku, Kyoto 606-8502, Japan

<sup>b</sup> Graduate School of Science and Engineering, Saitama University, 255 Shimo-Okubo, Sakura-ku, Saitama 338-8570, Japan



## ARTICLE INFO

### Article history:

Received 16 January 2022

Revised 12 June 2022

Accepted 13 June 2022

Available online 24 June 2022

### Keywords:

Oblique detonation

Two-stage light gas gun

Hydrogen

Non-uniform

## ABSTRACT

To the best of our knowledge, this study is the first to adopt an experimental approach for addressing the theoretical properties of sphere-induced oblique detonation in a non-uniform mixture. A stratified  $H_2/O_2$ -Ar mixture was supplied with a concentration gradient normal to the launching direction of a two-stage light gas gun. High-speed schlieren images were taken to study the morphologies of oblique detonation. The waiting time after the  $H_2$  injection until the launch was varied to investigate the effect of the concentration gradient. Oblique detonations were successfully formed in every condition considered with curved wave fronts and Chapman-Jouguet detonations were partially achieved. However, stronger concentration gradients induced several critical structures, such as local quenching and a Straw-Hat structure. Also interestingly, a part of the detonation front in the region where the Chapman-Jouguet solution does not exist propagated relative to the projectile, whereas the rest remained steady. Moreover, analysis of several relevant physical length scales indicated that the nondimensional diameter, which is critical for initiating detonation in a uniform mixture, could be a valid criterion near the projectile, but not far from it. Instead, the wave curvature determined the local structures of oblique detonation, which quantitatively explained the velocity deficit and emergence of the critical structures. We believe the findings of this study will benefit the understanding of non-uniformly premixed detonation in a propagating form owing to its analogy to an oblique detonation.

© 2022 The Combustion Institute. Published by Elsevier Inc. All rights reserved.

## 1. Introduction

In recent years, increasing efforts have been made to understand the effects of non-uniform mixtures on detonation [1–7] for issues concerning non-ideal mixing that occurs in detonation-driven aerospace devices [6–9]. Vollmer et al. [1] observed Deflagration-to-Detonation Transition (DDT) in an obstructed channel filled with nonuniform hydrogen-air mixtures and found that DDT was sometimes unexpectedly more likely to occur in concentration gradients than in a uniform mixture. Boulal et al. [2] recently measured the instantaneous detonation velocity and cell width in concentration gradients parallel to the propagation direction, which matched those of a Chapman-Jouguet (C-J) detonation except for strongly nonuniform cases. These findings are crucial for aerospace vehicles with significantly limited mixing time [6–9]. This problem is equally important in the Oblique Detonation Wave Engine (ODWE), which is propelled by an oblique detonation wave (ODW) standing in the engine-frame fixed coordinate

system [10,11]. An ODW is formed when the flow speed exceeds its C-J velocity [12]; its wave structure is illustrated in Fig. 1. A self-sustained planar front behind a supporting body has a C-J velocity normal to the wave, for which its angle can be derived from the ratio of the C-J speed  $D_{CJ}$  to the flow speed (or the projectile velocity in the quiescent mixture)  $V_p$  as

$$\beta_{CJ} = \arcsin(D_{CJ}/V_p) \quad (1)$$

Although an abundance of previous research on the ODW have dealt with uniform mixtures [13–19], including experimental approaches using a light gas gun to launch a supersonic projectile into a detonable mixture, understanding on the non-uniformity effects on the ODW is far less than that on propagating detonation [13–17]. Until recently, only a few qualitative discussions on the effects of non-uniform mixtures have been reported in the literature [20–22]. Recent numerical work by Iwata et al. [23–25] and Fang et al. [26] addressed non-uniformly premixed ODW on a wedge/sphere, where several unique structures, such as a locally oscillating flame front [23] and a V-shaped flame edge [24–26], appeared. Nevertheless, only a few fundamental aspects are being understood. More progress is required to achieve a more comprehensive understanding. Also, due to the analogy of its spatial

\* Corresponding author.

E-mail address: [k.iwata@kusastro.kyoto-u.ac.jp](mailto:k.iwata@kusastro.kyoto-u.ac.jp) (K. Iwata).

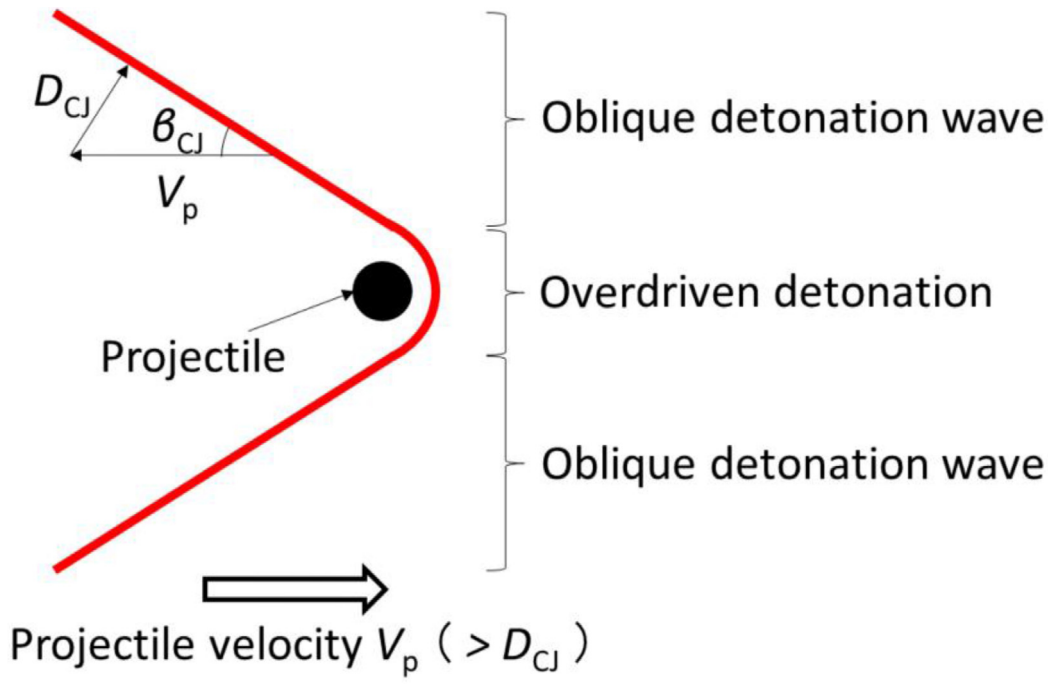


**Fig. 1.** Schematic of the oblique detonation wave (ODW).

structure to temporal variation of propagating detonation found by Matsuo et al. [27], physical insight into ODW directly benefits understanding of propagating detonation in various circumstances. Moreover, an ODW should be especially useful for theoretical analysis in non-uniform mixtures owing to its steadiness in the body-fixed frame and the common assumption of steady detonation in the associated theory.

In our most recent numerical work on non-uniform mixtures [28], we simulated a sphere-induced ODW in a non-uniform  $H_2$ - $O_2$ -Ar mixture to find curved wave fronts whose local wave angle was close to the C-J value. However, the velocity deficit was notable and detonation quenched in strongly fuel-rich mixtures. This study is the first to use an experimental counterpart to observe the non-uniformly premixed ODW using a two-stage light gas gun driven by hydrogen-oxygen detonation. A stratified  $H_2$ / $O_2$ -3Ar mixture was formed by injecting hydrogen into the observation chamber. The strength of the concentration gradient was controlled based on the waiting time after injection, and the observed phenomena were quantitatively analyzed according to several relevant physical length scales. Previous experiments on the ODW in uniform mixtures [14–16] verified the importance of the radius of curvature relative to the cell width in the initiation of the ODW, which should be all the more so in non-uniform mixtures owing to the curved wave structures observed previously [22–26,28]. This will further be a complicated issue owing to variable C-J velocity and variable cell width. Therefore, the authors have been motivated to discuss the local ODW structure based on the wave curvature effect.

## 2. Experimental methods

### 2.1. Two-stage light gas gun

**Fig. 2(a)** shows a schematic of a two-stage light gas gun belonging to Saitama University; its details are provided in [29]. A spherical projectile with a diameter of 9.52 mm was used. Driven by the detonation of stoichiometric hydrogen-oxygen filled at a pressure of 480 kPa, high-pressure helium gas compressed by a free piston

accelerated the projectile to a velocity  $V_p \approx 1800$ –2200 m/s at the entrance of the observation chamber. The projectile velocity was almost constant during the flight through the chamber with fluctuations of several tens of m/s.

Details of the observation chamber are depicted in **Fig. 2(b)**. It comprises a 143 mm circular cross-section perpendicular to the launching direction. A non-uniform mixture (and a uniform mixture for a complementary study) was filled in the chamber composed of hydrogen and a constant-composition oxidizer  $O_2$ +3Ar. The ODW formed in the mixture around the projectile was optically accessible in the lateral direction through a pair of 141 mm diameter BK7 windows. A high-speed camera ULTRA Cam HS-106E (NAC) was used to take high-speed schlieren photography of the ODW, which was triggered by the passage of the projectile across diode lasers in the first dump tank upstream of the observation chamber. The frame rate was set to 500,000 fps with an exposure time of 300 ns, resolving an area of 103 × 90 mm with 412 × 360 pixels.

### 2.2. Supplying system of a non-uniform mixture

**Fig. 3** illustrates an overview of the supplying system of a non-uniform mixture. Fuel and oxidizer were separately supplied in the experiments for the non-uniform mixture: oxidizer mixture  $O_2$ +3Ar was supplied to the observation chamber first at a prescribed partial pressure, and hydrogen stored in four separate tanks was supplied next through side-slit injectors equipped at the top of the chamber until a constant total pressure of  $70.0 \pm 0.6$  kPa was reached. By supplying hydrogen from a higher position, the buoyancy-driven flow created a nearly vertical concentration gradient, which will be proved later. Turbulent mixing during and shortly after the injection and molecular diffusion later governed the evolution of the hydrogen distribution toward uniformity. The pressure was monitored using a digital pressure sensor VUS-31-NV-01 (PISCO), which triggered a solenoid valve to control four pneumatic valves for injection control. Thus, a total composition of  $2H_2+O_2+3Ar$  was assured with an uncertainty of equivalence ratio  $\Phi=1.00 \pm 0.04$ . The strength of the concentration gradient at

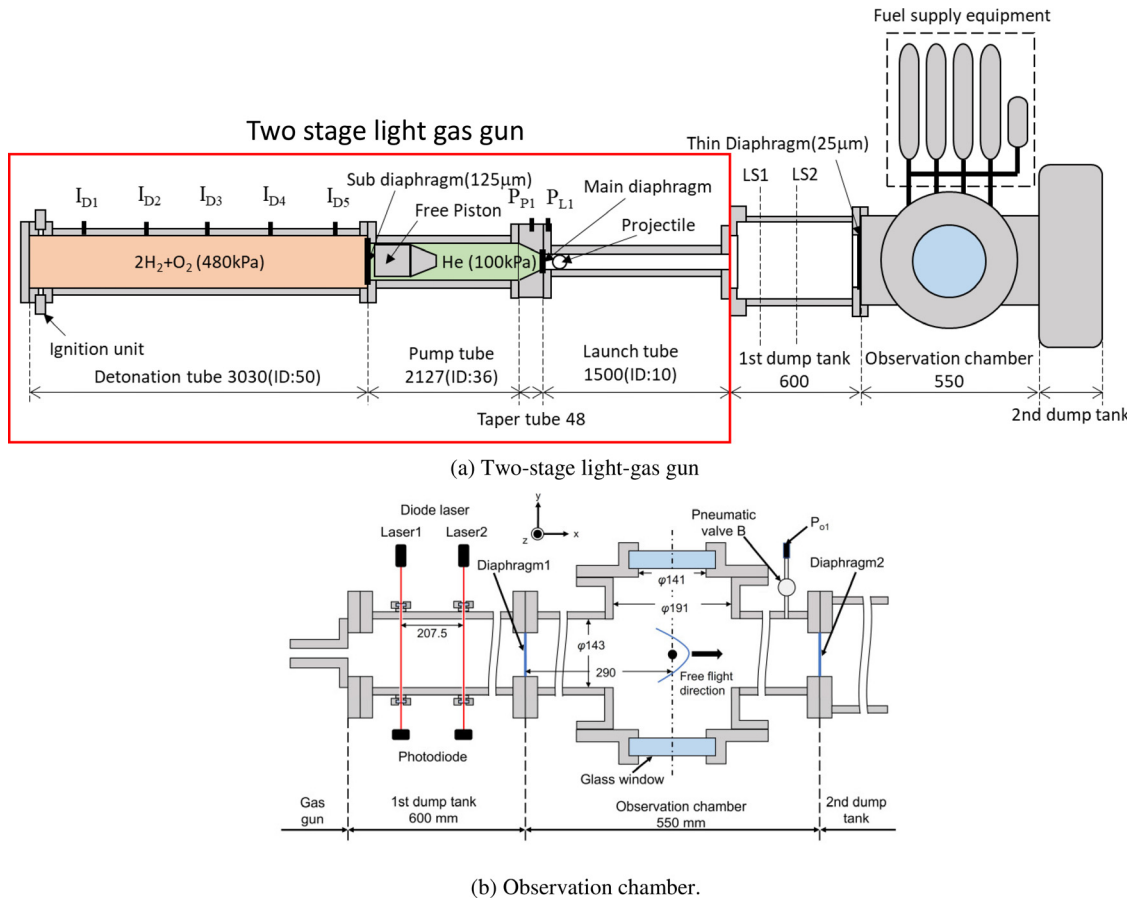


Fig. 2. Experimental apparatus.

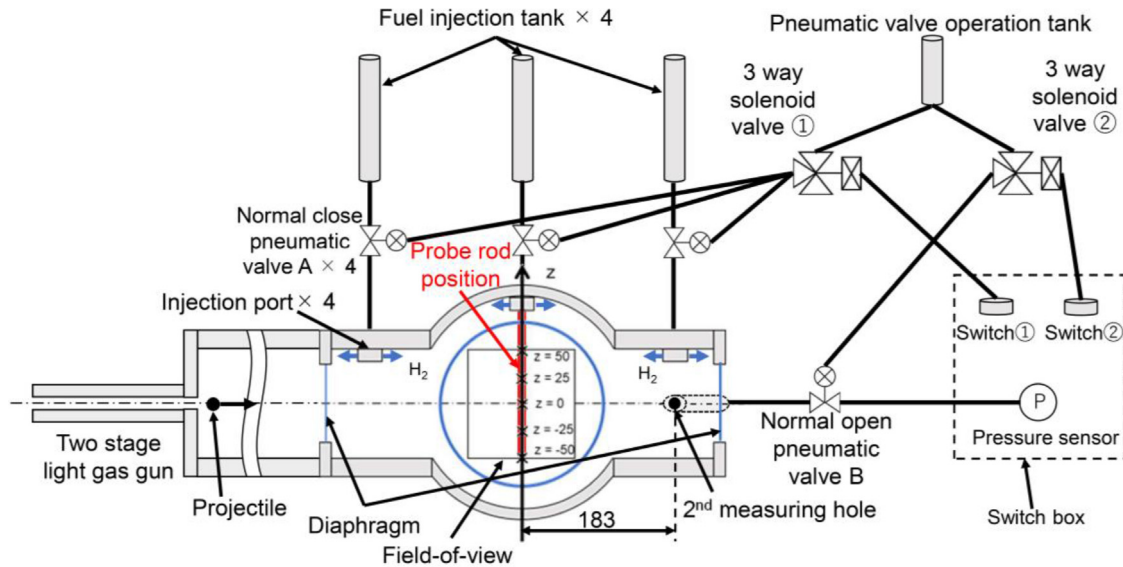
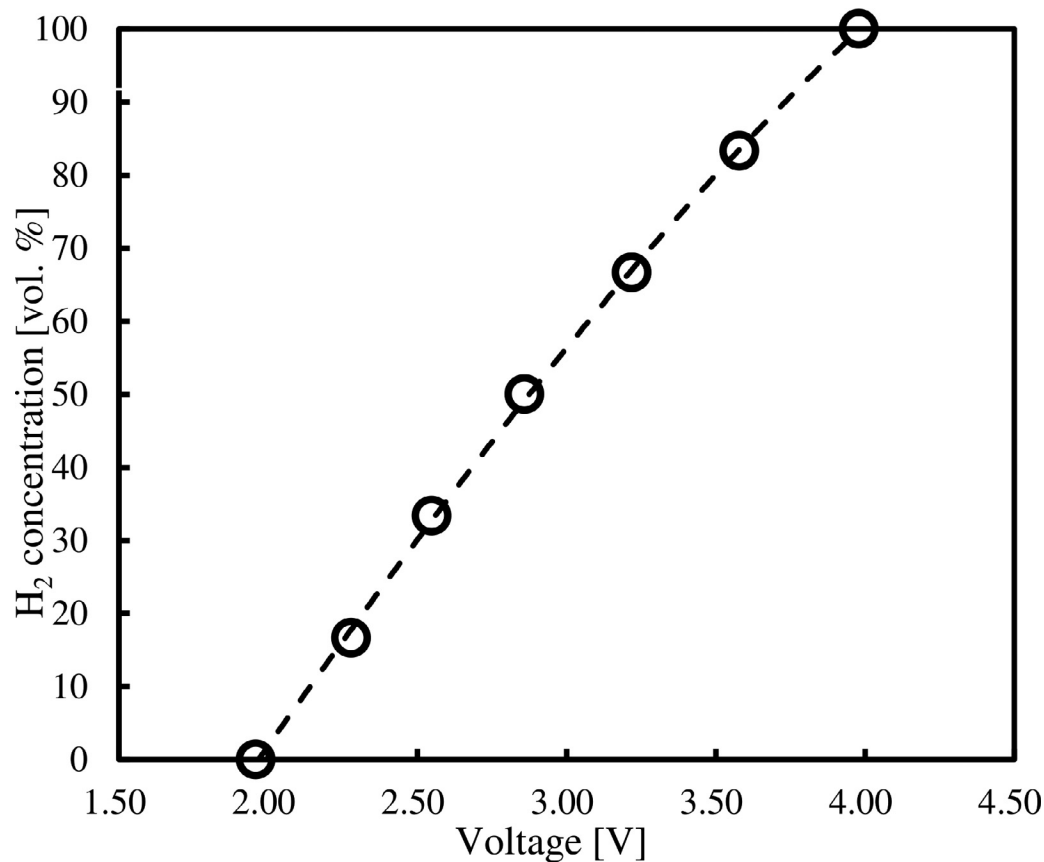


Fig. 3. Supplying system of a non-uniform mixture.

the time of launch was controlled by the time interval from the end of injection to ignition in the detonation tube. As described later, this supplying procedure promised a high reproducibility of the spatial/temporal profile of volumetric concentration of hydrogen  $\approx 0.5\%$  and a good vertical concentration gradient with minimal horizontal non-uniformity.

Detonation experiments were also conducted using uniform mixtures at the same pressure 70.0 kPa with the range of equivalence ratio of  $0.3 \leq \Phi \leq 2.0$ . The cell width of the uniform mixture, which is important as the threshold of ODW initiation through the parameter  $d/\lambda$  [14–16], was measured in another experimental setup for propagating detonation using a soot foil in a  $25 \times 31$



**Fig. 4.** Calibration curve of the anemometer probe for hydrogen volumetric concentration.

mm<sup>2</sup> rectangular channel. The cellular patterns were printed on a 225-mm-long and 0.3-mm-thick aluminum plate.

### 2.3. Concentration measurement

A hot-wire anemometer probe 0251R-T5 amplified by CTA 1011 (Kanomax), which was originally designed to measure velocity through convective heat transfer rate, was used to measure the volumetric concentration of hydrogen. The heat transfer rate to the anemometer is described by King's law [30] as  $\Delta T(A+BU^n)$ , where  $\Delta T$  is the temperature difference between the probe and surrounding mixture,  $U$  is the convective velocity, exponent  $n$  is a constant, and coefficients  $A$  and  $B$  depend on the transport coefficients and the heat capacity of the mixture [30]. As will be shown later, the convective heat transfer was negligible in the measurement, and the heat transfer rate was reduced to  $A\Delta T$ . Therefore, the heat release rate primarily relied on heat conduction and depended on the transport properties of the mixture including heat conductivity. The transport properties of hydrogen and the oxidizer O<sub>2</sub>+3Ar are significantly different, for which the anemometer can detect the hydrogen concentration without being influenced by the convective velocity. Fig. 4 shows a calibration curve of the probe in quiescent uniform mixtures with variable H<sub>2</sub> volumetric fractions. The output voltage of the anemometer exhibited an almost linear correlation. The accuracy of the concentration measurement considering a calibration error (and reproducibility later described) was estimated to be  $\lesssim 1.5\%$ .

A complementary measurement replacing all the gasses by helium showed that the bulk flow velocity, which was expected to be 1–10 m/s close to the fuel injectors, had negligible influence, resulting in almost a flat temporal voltage profile exemplified in Fig. 5 (a vertical dotted line denotes the end of injection) well

within  $\pm 0.01$  V at the highest measurement location  $z = 50$  mm. This was partially because the injection velocity was damped soon after the end of the injection within a few seconds, as shown by the weak fluctuation of the output voltage around  $t_w=0\text{--}3$  s.

A calibrated probe was inserted at 5 different vertical positions along the center of the observation chamber at  $z=-50, -25, 0, 25$ , and 50 mm from the height of the projectile flight (Fig. 3). Because the probe wire had a diameter of 5  $\mu\text{m}$ , the spatial resolution of the measurement was sufficient. Moreover, the supporting rod with diameter 4.6 mm was significantly smaller than the dimensions of the chamber and, hence, did not disturb the flow field during the injection process. This was verified by a complementary simulation using Fire Dynamic Simulator (FDS) [31] including the rod structure.

The concentration measurement and the launching experiment were conducted at separate times, and hence assuring reproducibility of the spatial/temporal profile of hydrogen concentration is vital for the quantitative study of the observed ODW. In addition to this, the verticality (one-dimensionality) of the concentration gradient is also a requisite to observe a steady ODW during the horizontal flight of the projectile. To verify these important qualities, measurement was conducted repeatedly and at another horizontal location. The first test and the second test in Fig. 6 depict the temporal profiles of the hydrogen concentration in the two separate tests measured at  $z = 0$  mm. Although the difference in the vertical scale of the data recorder made the second result appear noisy, they agreed with each other with an error  $\approx 0.5\%$  in volumetric fraction.

The concentration measurement was also conducted at another horizontal position at a distance of 183 mm in the launching direction (the second measuring hole in Fig. 3). Unfortunately, the output voltage was contaminated by severe low-frequency noise ow-

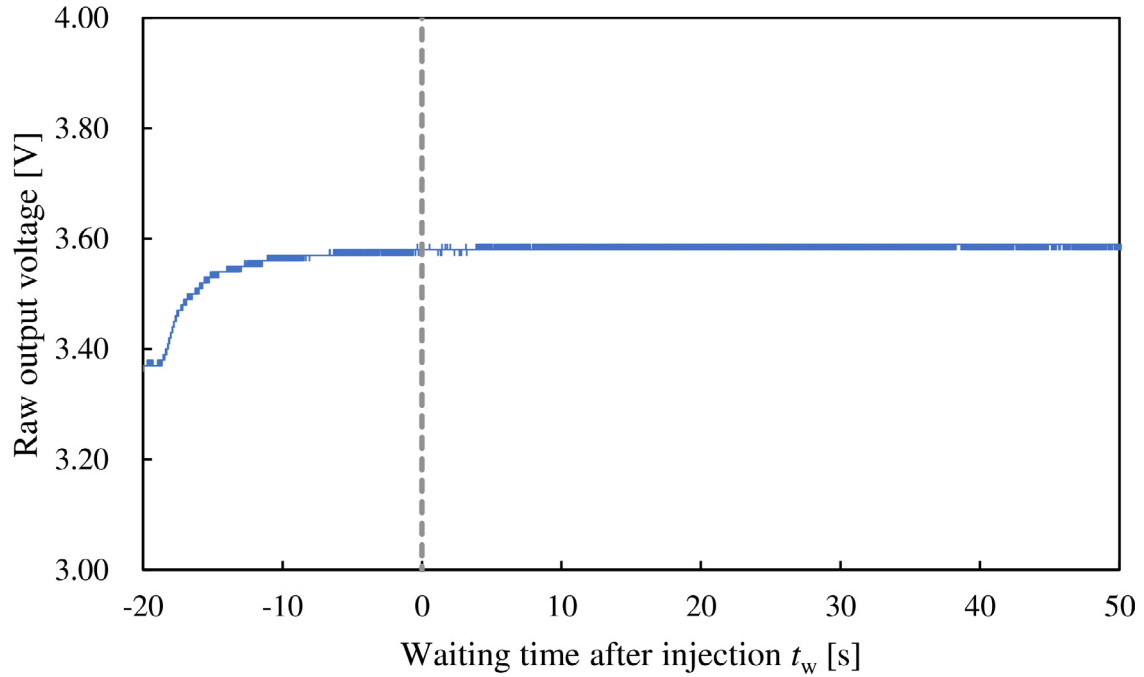


**Fig. 5.** Temporal evolution of raw output voltage in complementary anemometer measurement using only helium.

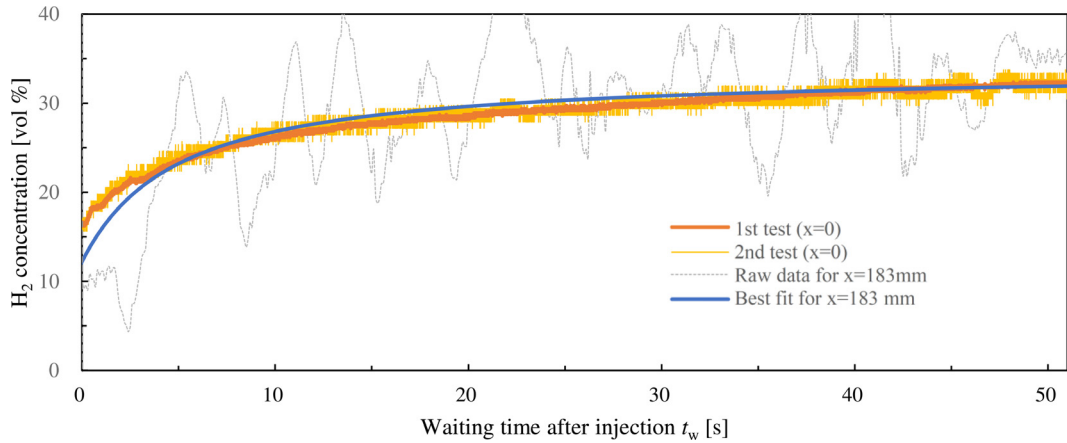


**Fig. 6.** Measured temporal evolutions of hydrogen concentration at  $z = 0$  mm.

ing to the probe supporting structure. Therefore, it was low-pass filtered and best fitted by an exponential convergence, as shown by the blue line in Fig. 6. Since it was far from the injectors, the concentration at the end of injection was lower than that at the center of the chamber, but it increased rapidly and soon approached the central concentration around  $t_w = 5$  s. The difference after  $t_w = 5$  s was well within 2%. A roughly tuned FDS simulation [31] also supported this minor horizontal nonuniformity and predicted a negligible horizontal gradient throughout the field of view. Furthermore, as will be proved later, the ODW in the nonuniform mixture was steady during the flight through the test chamber, except for intrinsically unsteady cases where propagating detonation appeared. These results are persuasive enough hereafter to make a reasonable assumption of identical spatial concentration profiles at the same waiting time and of vertical concentration gradient.

Fig. 7 summarizes the spatial profiles of the measured local equivalence ratio at each measurement position  $z = -50$ – $50$  mm and waiting time  $t_w = 3, 5, 7, 10, 20$ , and  $30$  s from the end of injection, as blank symbols. Additionally, to support the measured gradient, the calculation results of the FDS 3D fluid-dynamic simu-

lation are illustrated by lines. FDS applies a low-Mach-number approximation to solve time-dependent problems efficiently and incorporates multi-component diffusion. Gravity was also considered for the buoyancy. In our simulations, a coarse resolution of 5 mm was chosen for computational efficiency, and the tuning parameters for turbulence modeling were all set constant in every simulation with the turbulent Schmidt number  $Sc = 0.2$ . Apparently, a good agreement between both results qualitatively supported the fact that the measurement provided an adequate description of the distribution of hydrogen. Although the agreement was worse at vertical positions that were higher than that of the projectile flight, this can be attributed to the sensitivity of the modeling of the flow close to the injectors, which is significantly affected by the turbulence modeling and probably by the mesh arrangement around the injectors. This difficulty in jet modeling is different from the work of Metrow et al. [32], where a flow driven primarily by molecular diffusion and buoyancy in a stratified layer was simulated. In the presently concerned waiting period, the local equivalence ratio ranged from  $\Phi = 0$  to around  $\Phi = 4$  in the field of view and gradually evolved until it approached a sinusoidal fashion, which was

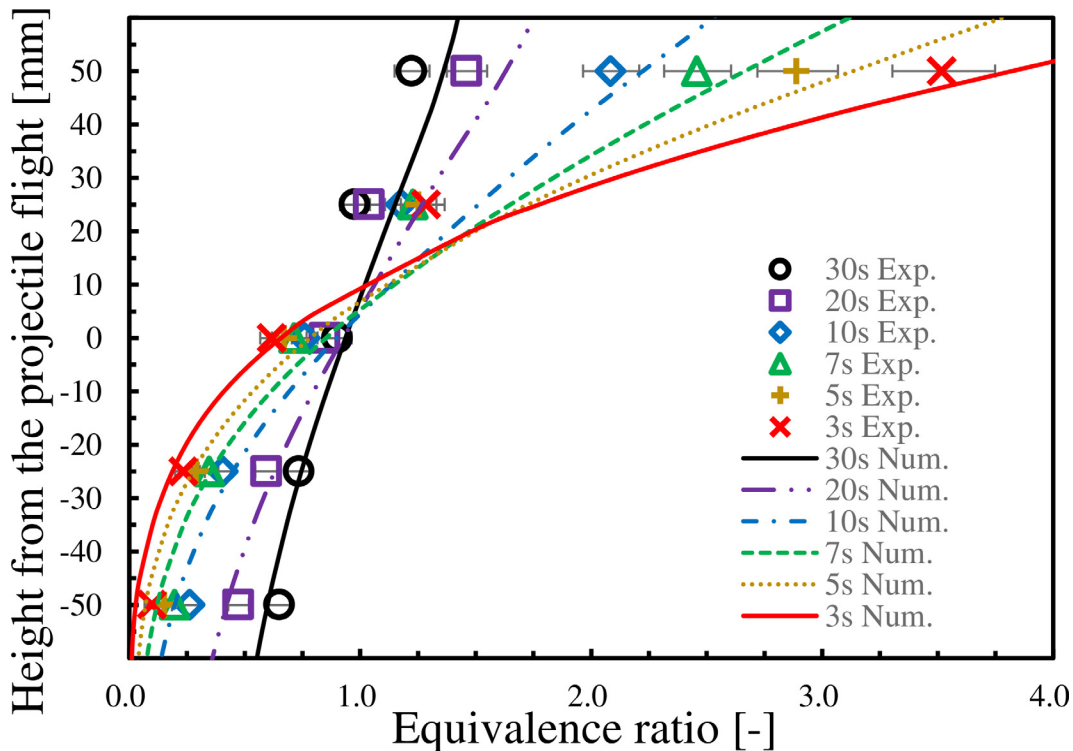


**Fig. 7.** Measured (symbols) and calculated (solid lines) spatial profiles of the local equivalence ratio at each waiting time.

similarly confirmed by Vollmer et al. [1] in an obstructed rectangular channel. It can be also noted that the local equivalence ratio at  $z = 0$  mm reached  $\Phi = 0.67$  ( $d/\lambda = 4.95$ ) at  $t_w = 5$  s and was already close to the converged value  $\Phi = 1.00$  ( $d/\lambda = 6.57$ ) in a few tens of seconds. Considering that  $d/\lambda \gtrsim 5$  is required to sustain stabilized ODW on a sphere in a uniform mixture [14],  $d/\lambda$  around the projectile at every waiting time  $\gtrsim 5$  s would exceed the threshold for the success of ODW in the context of uniform mixtures.

### 3. Results

#### 3.1. ODW in the uniform mixture

We started with ODW experiments using uniform mixtures that were prepared by filling a premixed mixture at  $70.0 \pm 0.6$  kPa. Fig. 8 shows four instantaneous pictures taken by Schlieren photography for mixtures with  $\Phi = 0.70$ , 1.00, 1.50, and 2.00. An ODW was successfully formed between  $\Phi = 0.70$ –1.50 (Figs. 8(a)–(c)), while decoupled shock-induced combustion in the Large-Disturbance-Regime (LDR) [18] resulted when  $\Phi = 2.00$  (Fig. 8(d)) and  $\Phi = 0.60$  (not shown here). Similarly,  $\Phi \leq 0.50$  resulted in steady shock-induced combustion (SIC, not shown here). Except in the cases with LDR oscillating behavior, all wave fronts were steady relative to the projectile during the projectile flight through the field of view. Minor differences between the wave angles of the ODW for each case reflect the relationship dictated by Eq. (1) considering  $D_{CJ}$  is strongly dependent on  $\Phi$ , as shown in Fig. 9, where the solid curve denotes a theoretical calculation with the use of DETON subroutine in CEA [33]. The symbols in the same figure are the velocities derived from the measured average wave angle of the ODW in each case using Eq. (1). Although the detonation velocity in each case matches the C-J value well, it is a few percent below the theoretical value owing to the wave-curvature-induced attenuation [34–35].

Fig. 10 summarizes the cell width of a uniform mixture at each equivalence ratio measured in the soot-foil experiment. Success of

ODW and failure as SIC in the launching experiment are distinguished by different symbols. The formation of the ODW is known to depend on  $d/\lambda$  [14–16]. As shown here, the critical cell width lies between  $\lambda = 1.9$  at  $\Phi = 1.50$  and  $\lambda = 2.2$  at  $\Phi = 0.60$ . Therefore, the critical nondimensional diameter  $d/\lambda$  is estimated to be between 4.3 and 4.9, which is reasonable for a mixture with higher cell regularity [14]. A fourth-order polynomial approximation was made, as denoted by the blue dotted curve in the figure, which will be referred to as the interpolated cell width for the range of equivalence ratio concerned.

#### 3.2. ODW in the non-uniform mixture

The waiting time after injection  $t_w$  was varied at the launching velocity  $V_p = 1800$ –2200 m/s. Fig. 11 shows instantaneous ODW structures observed at different waiting times of  $t_w = 5$ , 10, and 20 s.  $V_p$  in Figs. 11(a)–(c) was around 2200 m/s and 1854 m/s in Fig. 11(d) with fluctuations of 10–50 m/s. Hereinafter, the last case is termed the “low-velocity case,” and the rest are termed “high-velocity cases” and are referred to by their waiting time  $t_w$ . As shown in the figures, the ODW was successfully formed at all the waiting times, although several critical features appeared far from the projectile at shorter waiting times  $t_w \leq 10$  s. Furthermore, the ODWs in the three high-velocity cases were all steady throughout the flight, which reinforced the one-dimensionality of the concentration gradient, while the upper wave front in the low-velocity case propagated relative to the projectile, which was apparent in its temporal evolution, as separately shown in Fig. 12(a).

The steady ODW front in the high-velocity  $t_w = 20$  s case had a weak curvature, which was confirmed in our previous numerical study on wedge-induced ODW [24,25] and sphere-induced ODW in an axisymmetric gradient [28]. The convex and concave waves on the lower and upper sides, respectively, reflect the dependence of the C-J velocity on the hydrogen concentration, as shown in Fig. 9. (A quantitative discussion of this aspect is provided later.)

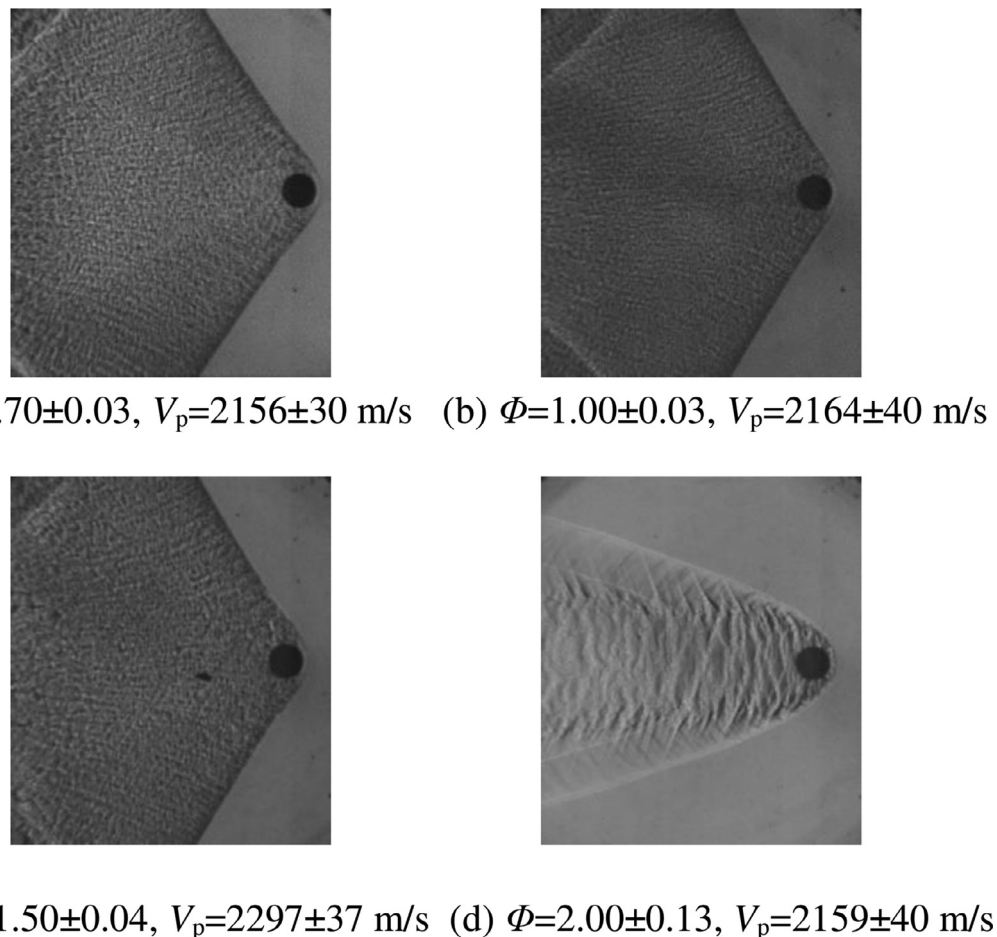


**Fig. 8.** Instantaneous pictures of ODWs and SIC in the uniform  $2\Phi\text{H}_2+\text{O}_2+3\text{Ar}$  mixture.

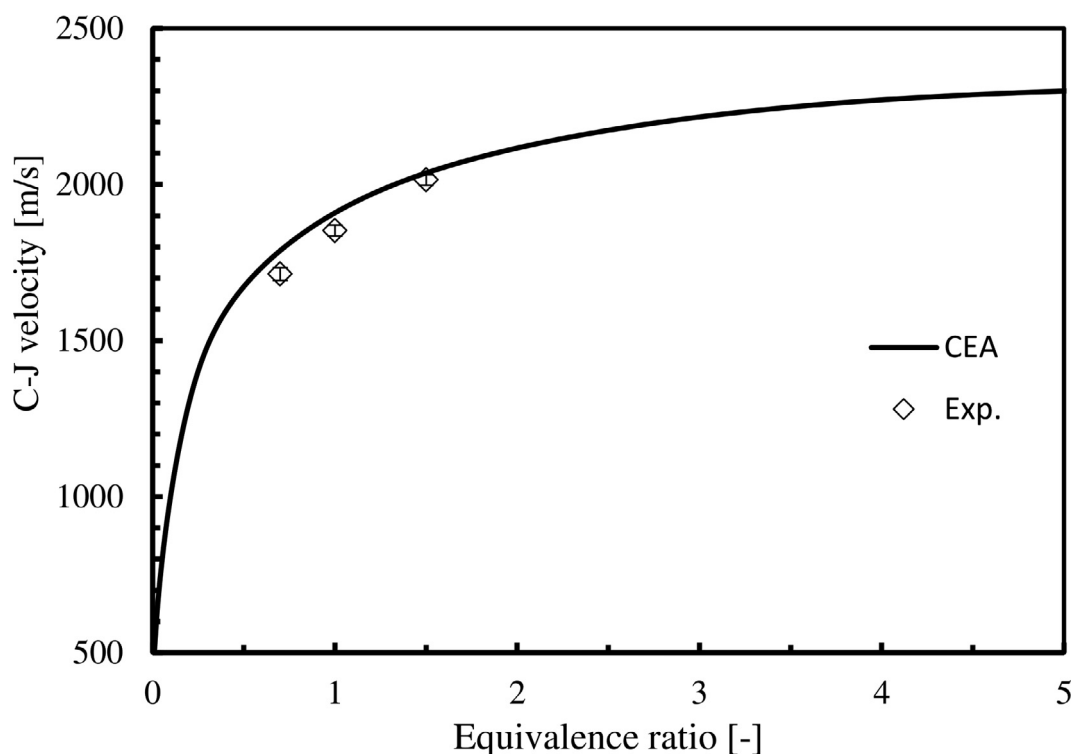


**Fig. 9.** C-J velocity of the  $2\Phi\text{H}_2+\text{O}_2+3\text{Ar}$  mixture for the variable equivalence ratio.

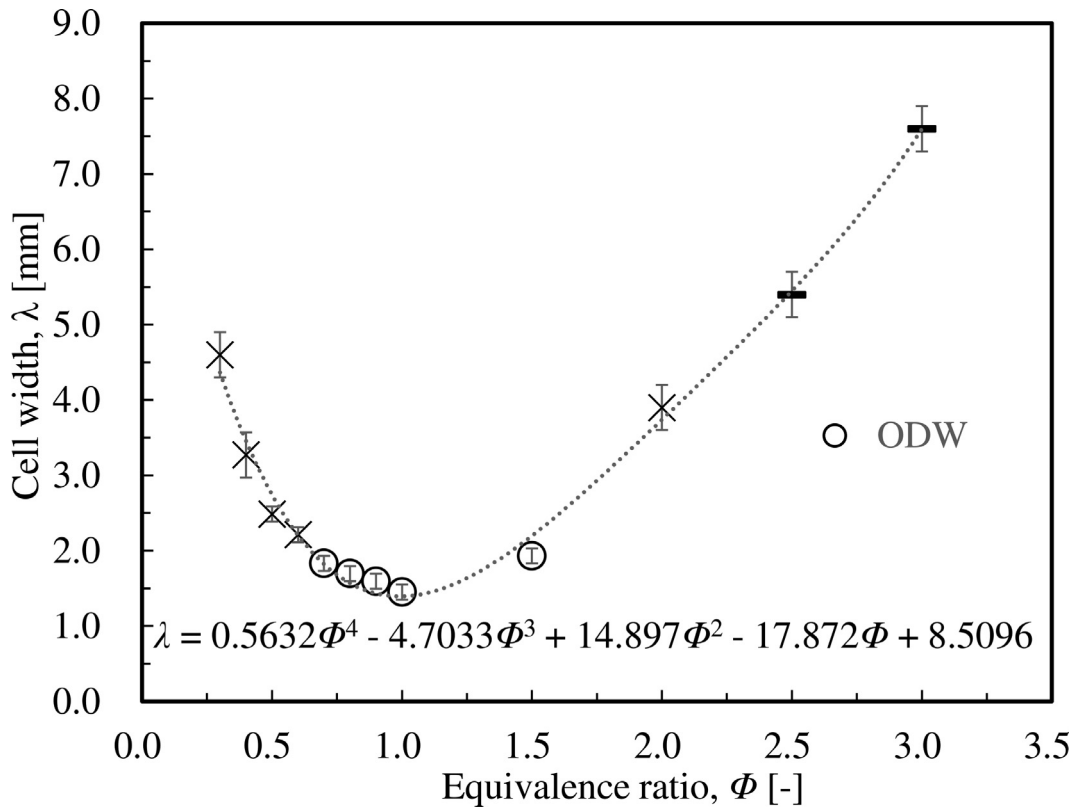


**Fig. 10.** Cell width measured in the soot-foil experiment: success/failure of the ODW is distinguished by different symbols, and no launching experiment was conducted for  $\Phi \geq 2.5$ .

A stronger concentration gradient at  $t_w=10$  s induced several critical structures. One feature was an inflection point of the wave front around  $z = 40$  mm (A in Fig. 11(b)), through which an outward increase in the wave angle turned into a sudden decrease. In contrast, the wave angle increased suddenly through another inflection point at approximately  $z=-30$  mm (B in Fig. 11(b)). Weak unsteadiness was observed here, which resembled the local explosion phenomenon occurring in the Straw-Hat structure [14]. Transition to detonation is known to be induced by this local explosion, for which it is implied that a transition to an ODW front occurred here. These two inflection points thus indicate that the ODW in this case was in a marginal state close to quenching. Another thing to note, which is similarly true for the  $t_w=5$  s case, is that the cellular patterns were prominently rougher around these critical structures, thereby indicating that some physical scales become comparable with the cell width to induce these phenomena. Since the local equivalence ratio grows farther from unity away from the projectile, as shown in Fig. 7, this trend also agrees with the dependence of cell width (Fig. 10).

At  $t_w=5$  s with the strongest concentration gradient (Fig. 11(c)), quenching of the ODW occurred around  $z = 40$  mm (C in the figure), where the shock and flame decoupled upward. A reduction in the wave angle occurred suddenly, similar to that observed in  $t_w=10$  s around a similar height. Therefore, it is indicated that a critical phenomenon similar to or the same as the quenching occurred at the upper inflection point A in Fig. 11(b), but in a more discreet manner. Our recent numerical work on the non-uniform ODW [28] also predicted a similar quenching phenomenon in a strongly fuel-rich mixture in stronger concentration gradients. Therefore, our numerical prediction is qualitatively validated by the present observation, and this type of local quenching could be common in a strongly non-uniform mixture, like that formed in detonation engines. On the other hand, there was no evidence of ODW formation on the lower side wave front. However, close

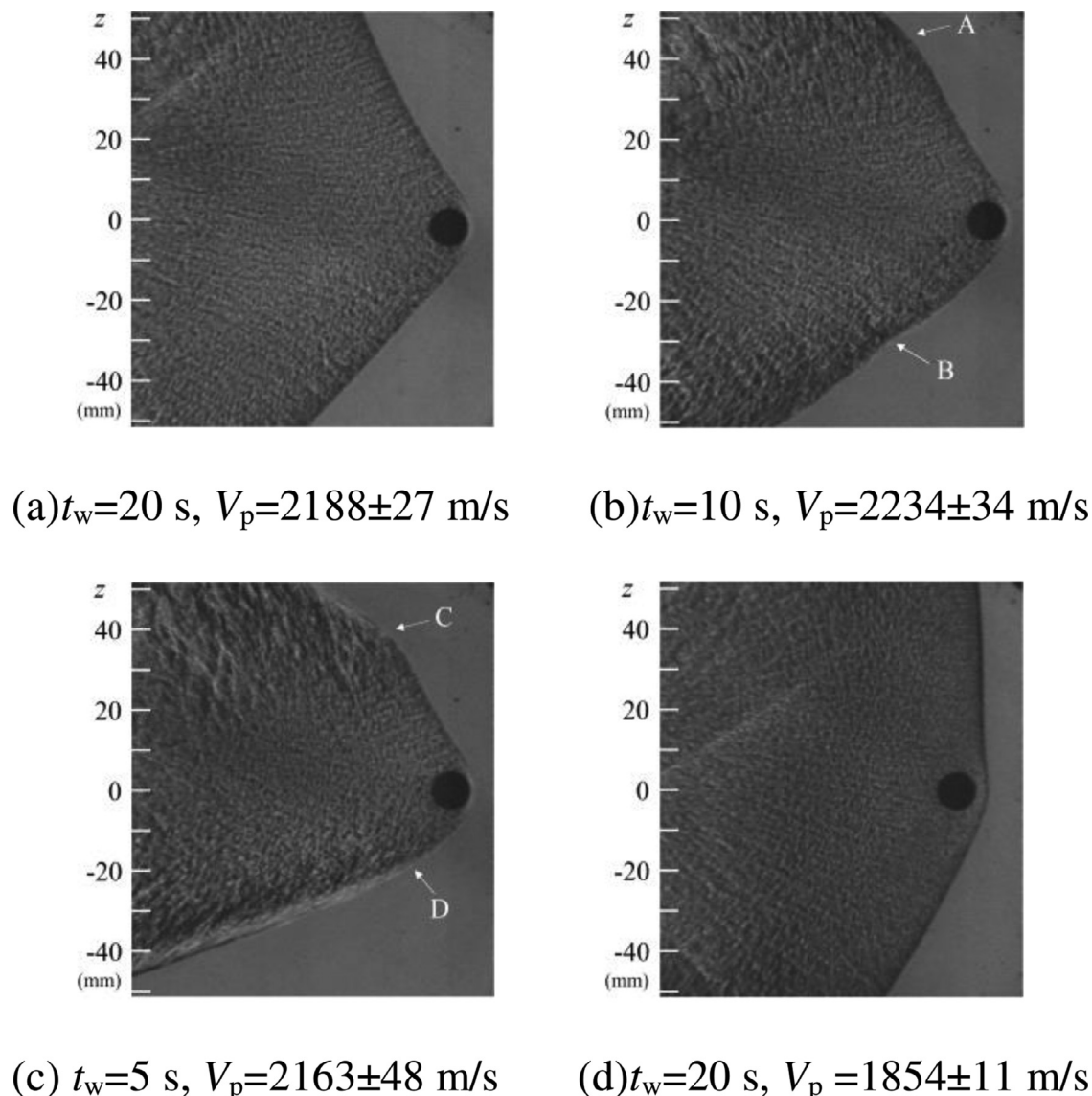
to the projectile (upstream of D in the figure), there seems a coupling of the shock and flame resembling ODW. Nonetheless, as will be proved later, this can be merely regarded as a strong bow-shock induced flame. Similarly, the lower wave front upstream of the local explosion at  $t_w=10$  s (Fig. 11(b)) can be rather regarded as a strong bow-shock induced combustion, but as a precursor to the transition at point B in this case.

Fig. 12 illustrates a peculiar phenomenon in the low-velocity  $t_w=20$  s case in which the upper wave front propagated relative to the projectile and converged into a normal detonation wave. It is also interesting that the lower wave front remained steady during the flight in the field of view. As proved by a superimposed image of each instantaneous wave picture (Fig. 12(b)), the higher the wave front is, the faster the wave propagated, in contrast to the overdriven region close to the projectile which remained less unsteady. These results agree with the trend of the C-J velocity dependence on the hydrogen concentration. For instance, considering the C-J velocity at  $z = 50$  mm is 2032 m/s for  $\Phi=1.48$ , relative velocity is estimated to be  $\approx 200$  m/s, and the C-J velocity at  $z = 25$  mm is 1919 m/s for  $\Phi=1.03$ , resulting in a relative velocity  $\approx 60$  m/s. Although these relative velocities did not match the wave movement at earlier times ( $\Delta t=108-128$   $\mu$ s from the triggering of the high-speed camera), they matched in order around  $\Delta t=128-138$   $\mu$ s. However, the agreement was still insignificant owing to the transient behavior of the curvature effect (weakening as the wave approached normal) and an out-of-plane 3D structure.

## 4. Discussion

### 4.1. Three-dimensional geometry of the ODW

In uniform mixtures, the physics of the ODW around a spherical projectile can be treated in the context of an axisymmetric problem. However, the one-dimensional concentration gradient



**Fig. 11.** Instantaneous pictures of ODWs in non-uniform  $2\text{H}_2+\text{O}_2+3\text{Ar}$  mixtures.

considered in the present study makes it essentially three dimensional. For a quantitative discussion of the theoretical properties of the ODW, this three dimensionality makes it difficult to evaluate the curvature effect on the detonation velocity deficit; out-of-plane wave curvature cannot be estimated accurately considering the axisymmetric value  $\cos\beta/z$  at height  $z$  from the projectile on the ODW front [16] is not necessarily appropriate.

Therefore, some remarks on its 3D structure are provided in advance through a simplified geometrical analysis. Fig. 13 shows a schematic describing geometrical variables used in the analysis. In this geometrical consideration, the independent variables that represent the ODW surface in 3D space were taken to be  $(x, \theta)$ , where  $x$  is positive in the launching direction and  $\theta$  is the azimuth in the  $(y, z)$  plane. The position vector  $p$  on the ODW surface was thereby represented as  $p(x, \theta)=(x, y(x, \theta), z(x, \theta))$ . Only one constraint must be satisfied for the normal vector to the ODW surface  $\nu$ :

$$V_p \mathbf{e}_x \cdot \nu = D \quad (2)$$

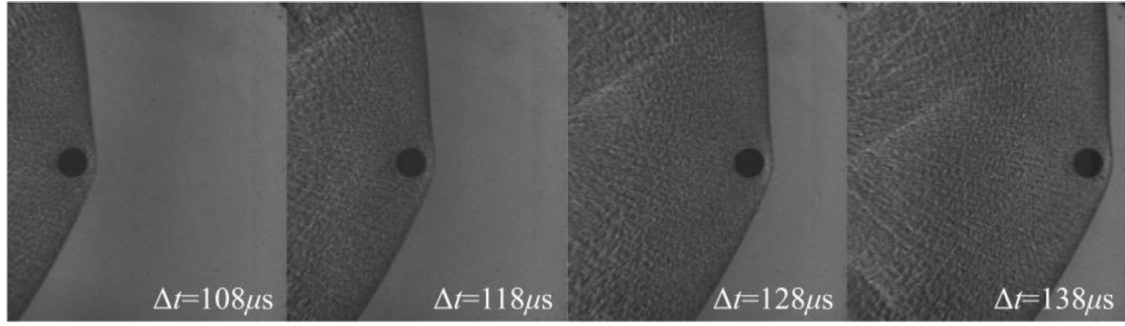
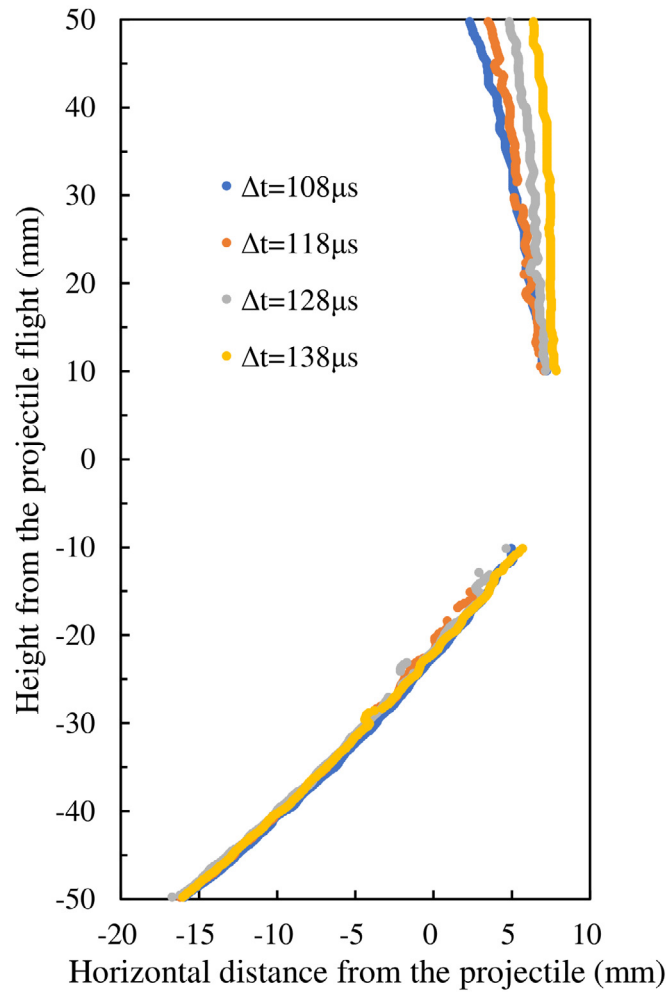
where  $\mathbf{e}_x$  is a unit vector in the launch direction. The above equation is the 3D counterpart of Eq. (1), and means that the component of the projectile velocity normal to the ODW surface at each

position must be balanced against the detonation velocity  $D$ . Here,  $D$  at each position was calculated using the following formula proposed by Nakayama et al. [34–35], which considers the curvature effect:

$$D = f(\kappa\lambda)gD_{CJ} \quad (3)$$

where  $f$  is a cubic polynomial function of the non-dimensional curvature  $\kappa\lambda$ :  $f(x)=1-1.3017x+16.089x^2-169.67x^3$  [35]. The degree of overdrive function  $g$  was defined close to the projectile, which was configured so that  $D=V_p$  in front of the projectile and exponentially decays to unity at  $x=-d/2$ . Since the concentration gradient is one dimensional in the  $z$ -direction,  $D_{CJ}=D_{CJ}(z)$ ; the local equivalence ratio  $\Phi$  is given as  $\Phi=\Phi(z)$ . Therefore,  $\lambda=\lambda(z)$  is also satisfied and derived from the same polynomial shown in Fig. 10. The 3D mean curvature  $\kappa$  is expressed as

$$\begin{aligned} \kappa &= \frac{1}{2} \frac{EN + GL - 2FM}{EG - F^2} \\ E &= \mathbf{p}_x \cdot \mathbf{p}_x, F = \mathbf{p}_x \cdot \mathbf{p}_\theta, G = \mathbf{p}_\theta \cdot \mathbf{p}_\theta, \\ L &= \mathbf{p}_x \cdot \nu_x, M = \mathbf{p}_x \cdot \nu_\theta, N = \mathbf{p}_\theta \cdot \nu_\theta \end{aligned} \quad (4)$$

(a) Successive schlieren images at a time increment of  $10 \mu\text{s}$ .

(b) Superposition of wave front position relative to the projectile at each moment.

**Fig. 12.** Temporal evolution of the ODW front at the low-velocity  $t_w = 20 \text{ s}$  case ( $V_p = 1854 \text{ m/s}$ ).

where  $E$ ,  $F$ , and  $G$  are the first fundamental values,  $L$ ,  $M$ , and  $N$  are the second fundamental values, and the subscripts denote partial derivatives by each coordinate that were obtained by the second-order central difference on the ODW surface. Spatial integration of the position vector on the ODW surface  $p=(x,y,z)$  was started at the nose of the normal overdriven detonation front and advanced in the negative  $x$  direction (behind the projectile) along the constant  $\theta$  line. The numerical procedure for the integration is described

below, which was derived from Eq. (2) based on the requirement  $v \cdot \mathbf{p}_x = 0$ :

$$p_{i+1,j} = p_{i,j} + dx \left( 1, \tan \beta_{i,j} \sin \theta_j / \cos(\theta_j - \alpha_{i,j}), \tan \beta_{i,j} \cos \theta_j / \cos(\theta_j - \alpha_{i,j}) \right) \quad (5)$$

where  $\beta$  is defined in a manner similar to Eq. (1),  $\beta = \arcsin(D/V_p)$ , and  $\alpha$  is the inclination angle of  $v$  projected on the  $y$ - $z$  cross-sectional curve of the ODW front in the azimuthal direction  $\theta$  (see

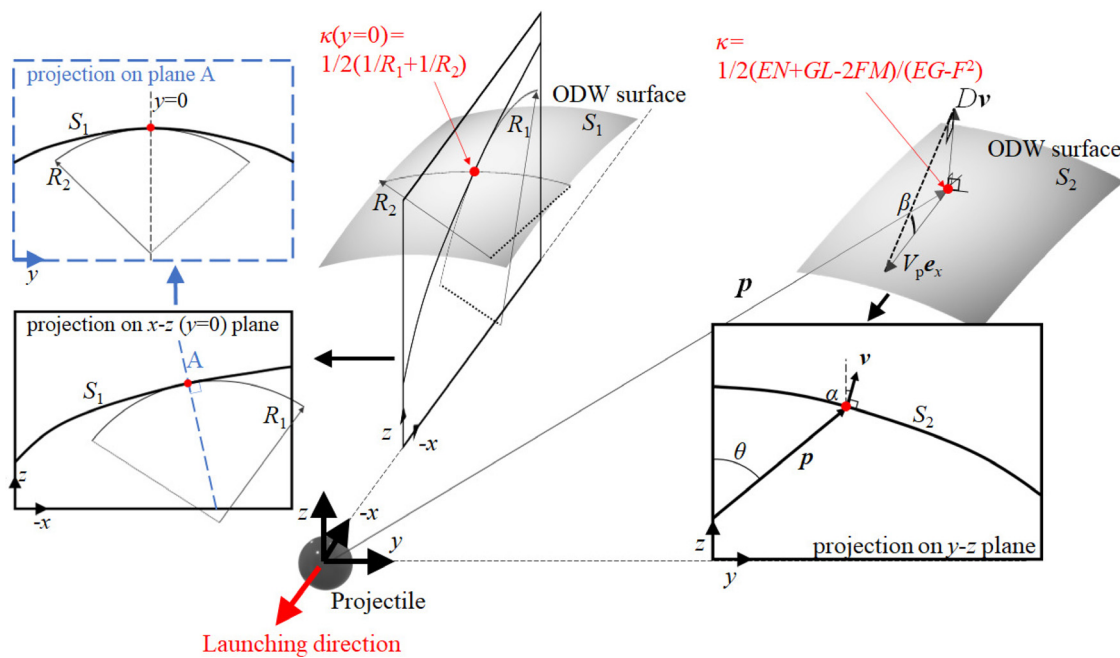


Fig. 13. Definitions of variables in the present geometrical analysis.

Fig. 13 for their definitions).  $i$  and  $j$  are the indices for the discretized grids in  $x$  and  $\theta$  directions, respectively, and  $\alpha$  was calculated by the second-order central difference on the  $y$ - $z$  cross-sectional curve. In a uniform mixture, this curve is a circle and  $\alpha=0$  is always satisfied.  $dx$  was here taken to be constant  $dx=-10 \mu\text{m}$ . A total of 3600 points were used to discretize uniformly in the  $\theta$  direction.

Since 3D mean curvature  $\kappa$  had to be calculated after obtaining the ODW surface, it was iteratively evaluated to update  $D$  in Eq. (3), which was then used to recalculate the ODW surface. The convergence of the iterative solution was controlled by a small under-relaxation factor of 0.002 to update  $f$  in Eq. (3).

The converged solution thereby achieved for the high-velocity  $t_w=20 \text{ s}$  case is overviewed in Fig. 14(a) as a 3D skeletal surface. Although its general appearance does not differ significantly from that of a uniformly premixed ODW, which is axisymmetric, a concavely curved wave front is prominent in the upper region. Fig. 14(b) shows its projection on the  $x$ - $z$  plane and the experimental observation as blue and gray solid lines, respectively. The solution with  $f=1$  (for the C-J velocity) is denoted by a dashed curve. Thus, the agreement with the experimental observation is sufficient to validate our geometrical calculation, except for the lower wave front approximately  $x \approx -20 \text{ mm}$ , which is probably exacerbated by the uncertain hydrogen concentration over  $z=50 \text{ mm}$ ; it was extrapolated from the measurement in  $z < 50 \text{ mm}$ . Also, when the solution is compared with that of the C-J assumption, one can note that the curvature effect is necessary to provide a quantitative explanation on the observed ODW structure.

Fig. 14(c) shows the  $y$ - $z$  cross-sectional curves for each longitudinal location. Although each curve appears similar to a circle, it is not vertically symmetric, and its centroid shifted slightly in the positive  $z$  direction. The more downstream it is, the more asymmetric the  $y$ - $z$  cross-sectional curve, and the higher its centroid shifts.

The partial derivatives of  $p$  and  $v$  by  $x$  and  $\theta$  are normal to each other at  $y=0$  owing to the symmetry, for which  $F$  and  $M$  vanish and  $\kappa$  reduces to  $\kappa=1/2(L/E+N/G)=1/2(1/R_1+1/R_2)=1/2(\kappa_1+\kappa_2)$ :  $R_1=E/L$  and  $R_2=G/N$  are the in-plane ( $x$ - $z$  plane) and out-of-plane radii of

the curvature, respectively, as illustrated in Fig. 13. In a uniform mixture with an axisymmetric ODW, the center of the out-of-plane curvature is located on the  $x$  axis, for which  $R_2=R_{2\text{ax}}=z/\cos\beta$  is satisfied [16].  $\kappa_2=1/R_2$  thereby evaluated is shown in Fig. 14(d) by a solid line against the height from projectile flight. The dashed line denotes the axisymmetric curvature,  $\kappa_{2\text{ax}}=1/R_{2\text{ax}}$ . Apparently, these two curvatures are not quite different from each other, and their differences are well within a factor of 1.38 on the upper wave front. Meanwhile, the lower wave curvature is closer to the axisymmetric curvature within a factor of 1.14. This indicates that using  $\kappa_{2\text{ax}}$  as the out-of-plane curvature in non-uniform ODW does not incur major problems in quantitative discussion. In addition to these, it will turn out to be true later that applying  $\kappa_{2\text{ax}}$  suffices to quantitatively explain the velocity deficit and emergence of the critical phenomena. Therefore, the out-of-plane curvature in the experimental ODW is hereafter estimated as  $\kappa_{2\text{ax}}$ . This can also be well justified for the shorter waiting times, although their geometrical solutions (not shown here) are slightly worse in agreement owing to the critical wave structures, for which Eq. (2) is no longer satisfied.

#### 4.2. Local wave angles

We now focus on the theoretical properties of local ODW structures observed by investigating the local wave angles and several length scales, including the radius of curvature on an axisymmetric assumption, as justified previously. The wave angles were evaluated as the moving averages of those evaluated by a second-order central difference at each pixel on the ODW front. The time-averaged wave front throughout the visible flight was used for the evaluation in the high-velocity cases where the ODW front was almost steady during the observation, while a single instantaneous picture at  $\Delta t=138 \mu\text{s}$  was used instead in the low-velocity case owing to its unsteady behavior. In contrast, the theoretically predicted C-J angle  $\beta_{\text{CJ}}$  was evaluated from the projectile velocity  $V_p$  using Eq. (1), and the CEA program was used to compute the C-J velocity  $D_{\text{CJ}}$ . The local hydrogen concentration  $X_{\text{H}_2}$  as an argument was interpolated from the experimental measurement by approximating it with an empirical formula  $X_{\text{H}_2}=\exp(a(z_0-z)^{\gamma})$  pro-

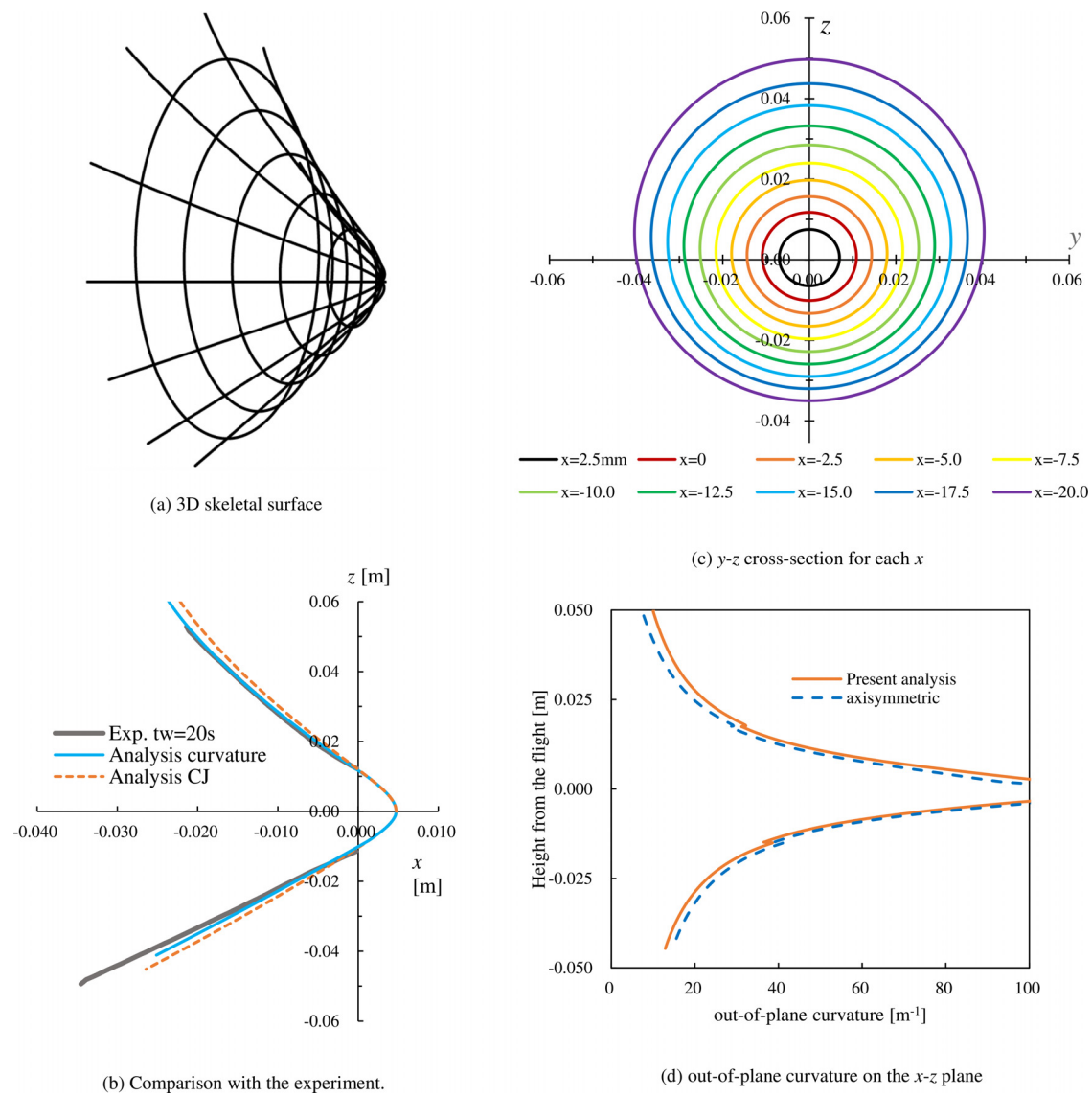


**Fig. 14.** Three-dimensional ODW structure at the high-velocity  $t_w=20$  s case ( $V_p=2188$  m/s) from the geometrical analysis.

posed by Karasawa et al. [36]. The evaluated experimental wave angles are shown as red circles in each of the left-hand graphs of Fig. 15 with black error bars  $\pm 1\sigma$ .  $\beta_{CJ}$  is denoted by a blue line with a light-colored band, illustrating the uncertainty of  $V_p$  and local hydrogen concentration. The corresponding schlieren image was placed next to the graph by matching its height to the ordinate of the graph.

What is seen to be common for the high-velocity cases (Figs. 15(a)–(c)) is that there exists a region above the projectile where the wave angle is almost equal to or slightly lower than the C–J value, i.e., a C–J detonation was realized. Particularly, good agreement was achieved entirely on the upper wave for the high-velocity  $t_w=20$  s case, except for a deficit region close to the overdriven region  $z \approx 10$ –20 mm that was induced by an expansion wave from the rear side of the projectile [15,16]. It is an interesting finding that the C–J theory could still be meaningful for non-uniform mixtures. However, the velocity deficit of the lower wave was notable. Nonetheless, its downward decreasing trend for  $t_w=20$  s (including the low-velocity case) was similar to that of  $\beta_{CJ}$ . For  $t_w=10$  s, the wave angle suddenly turned into a downward increase through the local explosion at point B in Fig. 11(b), but was still slightly lower than the C–J value. These deficits could

be attributed to the curvature effect, as will be demonstrated later.

Another thing easy to note here for the low-velocity case (Fig. 11(d)) is that the unsteadily moving upper wave described earlier in Fig. 12 is formed where the solution for Eq. (1) does not exist, i.e.,  $V_p < D_{CJ}$ . Therefore, the detonation wave here was proven to be no longer an ODW, but a normal propagating one.

For shorter waiting times  $t_w=5$  and 10 s, the critical inflection points denoted in Figs. 11(b) and (c) are both preceded by a sudden deviation from the C–J detonation slightly upstream. A similar deviating behavior was observed in the quenching phenomenon in our previous numerical study [28]: the ODW started to deviate from the C–J angle around a local equivalence ratio of  $\Phi \approx 1.5$ –2.0. The deviation in this experiment, when compared to the profile of the local equivalence ratio in Fig. 7, started at  $\Phi \approx 1.5$  for  $t_w=10$  s, and  $\Phi \approx 2.0$  for  $t_w=5$  s. Therefore, our experimental and numerical results quantitatively support each other in this critical phenomenon. For more insight into these and to distinguish whether the ODW or the SIC was formed locally, a quantitative discussion on several relevant physical scales is required, and will follow below.

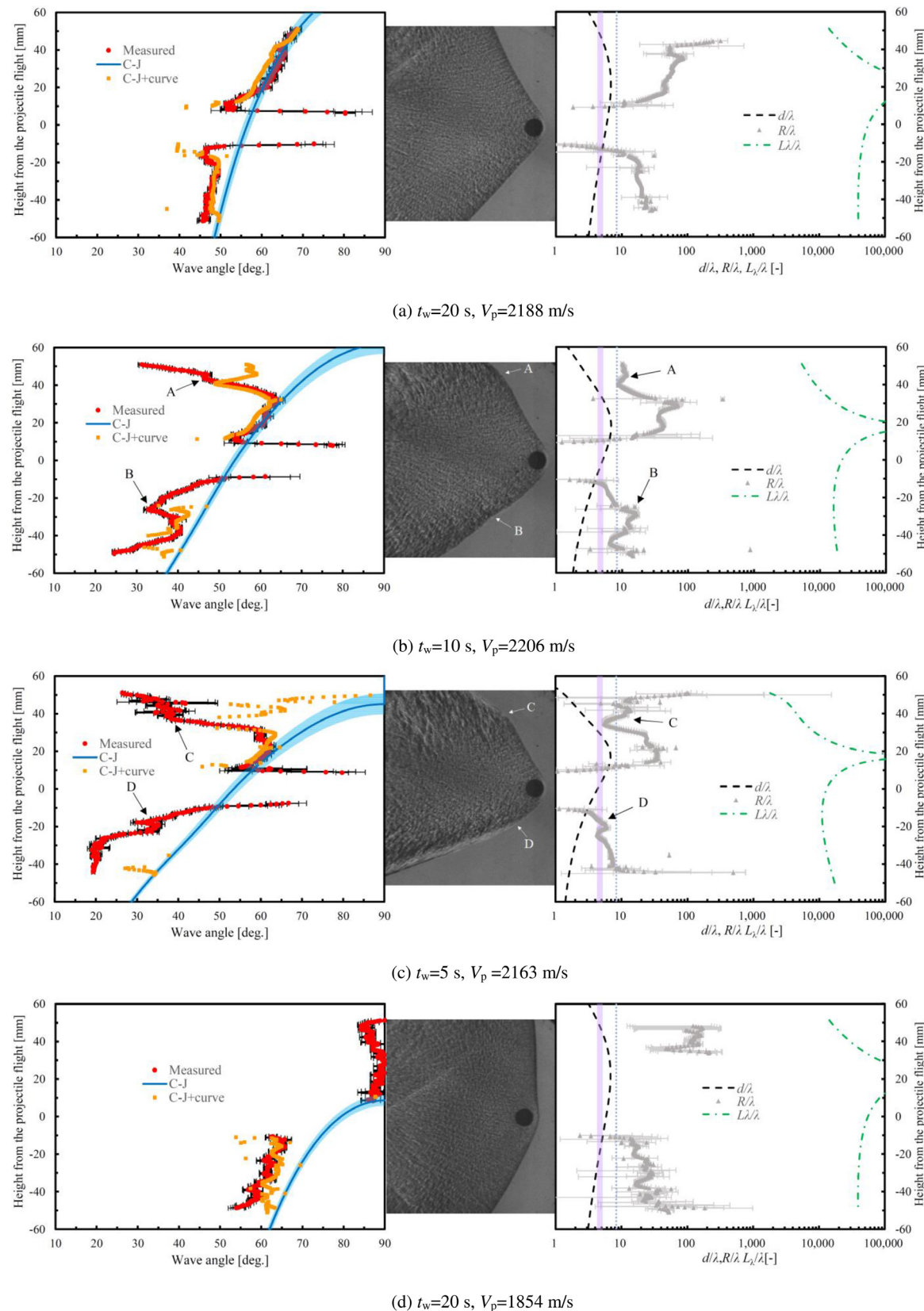


**Fig. 15.** Combined figures of the distributions of the wave angles (left hand), non-dimensional length scales (right hand), and corresponding schlieren image (center) with its height matched to the ordinates of the graphs. The measured wave angle (red circles), C-J theoretical wave angle (blue line with light-blue band as the uncertainty region), and C-J wave angle with the curvature effect included (orange squares) are shown in the left-hand side graph. The non-dimensional diameter  $d/\lambda$ , non-dimensional radius of curvature  $R/\lambda$ , and non-dimensional characteristic length of the concentration gradient  $L_\lambda/\lambda$  are shown in the right-hand side graph. The purple vertical solid and blue vertical dotted lines in the right-hand graph denote the critical values of the non-dimensional diameter and non-dimensional radius of curvature for ODW initiation, respectively.

### 4.3. Relevant physical length scales

A more in-depth analysis was performed on several relevant physical length scales, such as the projectile diameter  $d$ , 3D radius of curvature  $R$ , and characteristic length of the concentration gradient based on cell width  $L_\lambda$ , which are likely to influence the ODW structure. Specifically,  $L_\lambda$  is defined as  $L_\lambda = \lambda / (d\lambda/dz)$  and regarded as the characteristic length over which the cell width changes, which is an indicator of how strongly the concentration gradient alters the cellular structure. These physical length scales are represented in a non-dimensional form normalized by the cell width  $\lambda$ :  $d/\lambda$ ,  $R/\lambda$ ,  $L_\lambda/\lambda (=dz/d\lambda)$ .  $d/\lambda$  is known to be important for the criticality of ODW [14–16],  $R/\lambda$  is for the criticality of a wide range of detonation, and  $L_\lambda/\lambda$  was here evaluated to determine the magnitude of the change of the local cellular structure. The cell width was interpolated using the quartic formula shown in Fig. 10, and the in-plane curvature  $\kappa_1 = (\partial^2 z / \partial x^2) / (1 + (\partial z / \partial x)^2)^{3/2}$  was evaluated by the second-order central difference using the positions of the pixels on the ODW fronts.  $R$  was then obtained as  $R = 1/(2(\kappa_1 + \kappa_{2ax}))^{-1}$ .

The three nondimensional scales, namely,  $d/\lambda$ ,  $R/\lambda$ , and  $L_\lambda/\lambda$ , are indicated as a black dashed line, gray triangles with error bars, and a green dash-dotted line, respectively, in each of the right-hand graphs in Fig. 15. Their ordinate was matched to the height of the corresponding schlieren image next to the graph. Uncertainties of  $d/\lambda$  and  $L_\lambda/\lambda$ , which came from that of  $\lambda$ , were always sufficiently small to be within the thicknesses of the lines  $\sim 0.1$ . The threshold for the ODW initiation  $d/\lambda = 4.3\text{--}4.9$  is denoted by a vertical purple line, whose thickness is equal to its uncertainty, whereas the threshold value of  $R/\lambda$  is denoted by a vertical dotted line. Clearly,  $L_\lambda/\lambda$  is always significantly greater than unity by many orders of magnitude. Additionally, owing to the flat U-shaped variation of  $\lambda$  against the equivalence ratio, whose minimum is close to  $\Phi=1$  (Fig. 10), it diverges toward infinity around  $z \approx 20$  mm. Therefore, the concentration gradient itself was not strong enough to alter the cellular structure in this study.

The non-dimensional diameter  $d/\lambda$  around the projectile  $z \approx 0$  mm was above the threshold value of  $d/\lambda$  for  $t_w=20$  s and very close to the threshold for shorter waiting times. Therefore, the requirement for the formation of an ODW was barely satisfied for each condition in terms of a uniform mixture. In contrast, this length scale was no longer an indicator of the ODW success far from the projectile. Specifically, there was no evidence of quenching despite subcritical  $d/\lambda$  values in the lower wave front for  $t_w=20$  s. Although critical morphologies on the upper wave fronts at  $t_w=5$  and 10 s seem to coincide with the subcritical  $d/\lambda$ , these trends can be explained by using the radius of curvature  $R/\lambda$ , as will be mentioned later. Therefore, the non-dimensional diameter could still be important close to the projectile for ODW initiation, but not far from it. From the viewpoint of flame stabilization, it is thereby indicated that a mixture of a wider range of compositions can form an ODW in a non-uniform mixture free from the constraint on  $d/\lambda$  once initiated by a solid obstacle located in a more reactive mixture (with smaller cell width). This is similar in principle to stratified charge combustion in which the fuel distribution is arranged for spark ignition to work in a more reactive mixture, and it could also be a beneficial idea for detonation engines.

The radius of curvature, in contrast to the above two length scales, was proven to be crucial in the observed ODWs, as was partially indicated in the geometrical analysis (Fig. 14(b)), despite the relatively larger errors owing to the difficulty in evaluating the second derivative on discrete pixels. To quantitatively address the velocity deficit of an ODW, Eq. (3) was again invoked to account for the curvature effect, using  $R/\lambda (=1/\kappa\lambda)$  as an argument.  $g$  was here

set to unity. The detonation velocity thereby calculated was then converted to wave angle  $\beta_{CJ,c}$  through Eq. (1), which is plotted in Fig. 15 as scattered orange squares. Regions without the symbol experienced subcritical curvature (below the dotted line) so that the ODW could not be sustained or the curvature-induced quenching would be expected. Interestingly, as observed from the results,  $\beta_{CJ,c}$  agreed well with the experimental angles, especially on the lower wave fronts; it is excellent for  $t_w=20$  s, and relatively rough but still good for  $t_w=10$  s. Some partial disagreement was observed on the upper wave front, but it still explains the deviation from the C-J detonation close to the inflection points. Although slightly vague, the agreement upstream of inflection point A at  $t_w=10$  s was very good, but a trend was barely captured for inflection point C at  $t_w=5$  s. These agreements are sufficient to conclude that the ODWs in this study were primarily determined by the wave curvature, and several parts of the wave fronts with velocity deficit are within the definition of ODW: the entire lower front at  $t_w=20$  s, wave downstream of the local explosion at  $t_w=10$  s ( $z \approx -30$  to  $-40$  mm), and sub-C-J wave upstream of the inflection points A and C for  $t_w=5$  and 10 s, respectively. In contrast, the wave angle was significantly lower than  $\beta_{CJ,c}$  downstream of inflection points A and C, and the radius of curvature was subcritical upstream of local explosion B (the upstream part of the Straw-Hat structure); therefore, they cannot be ODWs. Similarly, the entire lower wave front at  $t_w=5$  s did not initiate an ODW and instead resulted in SIC.

It is surprising to note that the critical curvature reached close to critical locations A–C. Although it soon rebounded over the threshold downstream of A and C, an ODW was never recovered, i.e., detonation reinitiation failed. All these quantitative agreements reinforce the fact that the curvature effect created by the concentration gradient determines the detonation velocity of the ODW and its critical phenomena.

### Conclusion

In this study, the experimental observation of the ODW in non-uniform  $H_2/O_2+3Ar$  mixtures was conducted using a two-stage light gas gun launching a 9.52 mm diameter spherical projectile. A concentration gradient vertical to the launching direction was formed by injecting hydrogen into the oxidizer  $O_2+3Ar$ , and its strength was controlled by varying the waiting time before ignition. The results showed several interesting structures, among which curved wave fronts and several critical phenomena, including quenching and transition phenomena, were observed. Additionally, at a lower projectile velocity, a peculiar phenomenon occurred in which an ODW and an unsteady detonation front propagating relative to the projectile coexisted.

Several important findings from the analysis of several relevant length scales are that an ODW can be sustained at a local equivalence ratio where the non-dimensional diameter falls below the critical value for ODW formation, that C-J properties of the ODW are partially achieved at relatively milder wave curvature, and that the velocity deficit of a detonation wave and criticality of an ODW can be attributed to the curvature effect. Further efforts should be made to survey stronger concentration gradients in which the length scale of the concentration gradient is comparable to that of the cellular structure.

The analogy of oblique detonation with propagating detonation should provide useful insights into how a non-uniform mixture can influence the physics of detonation in various circumstances, and not just limited to the application of oblique detonations. Since the effect of mixing is now increasingly important in the application of aerospace propulsion devices such as the rotating detonation engines, we believe the findings of this study will provide important

insights into realistic detonation structures that are likely to occur in such applications.

### Declaration of Competing Interest

The authors declare that they have no known competing financial interests or personal relationships that could have appeared to influence the work reported in this paper.

### Acknowledgment

We would like to thank Editage ([www.editage.com](http://www.editage.com)) for English language editing.

### References

- [1] A. Matsuo, K. Fujii, detailed mechanism of the unsteady combustion around hypersonic projectiles, *AIAA J.* 34 (1996) 2082–2089.
- [2] A. St. George, R. Driscoll, V. Anand, E. Gutmark, On the existence and multiplicity of rotating detonations, *Proc. Combust. Inst.* 36 (2017) 2691–2698.
- [3] C. Li, K. Kailasanath, E.S. Oran, Detonation structures behind oblique shocks, *Phys. Fluids*. 6 (1994) 1600–1611.
- [4] C. Metrow, V.Y.A. Mozhdehe, G. Ciccarelli, Detonation propagation across a stratified layer with a diffuse interface, *Proc. Combust. Inst.* 38 (2021) 3565–3574.
- [5] D.H. Lieberman, J.E. Shepherd, Detonation interaction with a diffuse interface and subsequent chemical reaction, *Shock Waves* 16 (2017) 421–429.
- [6] H.F. Lehr, Experiments on shock-induced combustion, *Astronaut. Acta* 17 (1972) 589–597.
- [7] H. Nakayama, J. Kasahara, A. Matsuo, I. Funaki, Front shock behavior of stable curved detonation waves in rectangular-cross-section curved channels, *Proc. Combust. Inst.* 34 (2013) 1939–1947.
- [8] H. Nakayama, T. Moriya, J. Kasahara, A. Matsuo, Y. Sasamoto, I. Funaki, Stable detonation wave propagation in rectangular cross-section curved channels, *Combust. Flame* 159 (2012) 859–869.
- [9] I.Q. Andrus, M.D. Polanka, P.I. King, F.R. Schauer, J.L. Hoke, Experimentation of premixed rotating detonation engine using variable slot feed plenum, *J. Propuls. Pow.* 33 (2017) 1448–1458.
- [10] J. Fujii, Y. Kumazawa, A. Matsuo, S. Nakagami, K. Matsuoka, J. Kasahara, Numerical investigation on velocity deficit of detonation wave in RDE chamber, *Proc. Combust. Inst.* 36 (2017) 2665–2672.
- [11] J.L. Cambier, H. Adelman, G.P. Menees, Numerical simulation of an oblique detonation wave engine, *Jet Propuls.* 6 (1990) 315–323.
- [12] J.P. Sislian, R. Dudebout, J.M.I. Schumacher, T. Redford, Incomplete mixing and off-design effects on shock-induced combustion ramjet performance, *J. Propuls. Pow.* 16 (2000) 41–48.
- [13] J. Sun, J. Zhou, S. Liu, Z. Lin, Numerical investigation of a rotating detonation engine under premixed/non-premixed conditions, *Acta Astronaut.* 152 (2018) 630–638.
- [14] J. Verreault, A.J. Higgins, Initiation of detonation by conical projectiles, *Proc. Combust. Inst.* 33 (2011) 2311–2318.
- [15] K.G. Vollmer, F. Ettner, T. Sattelmayer, Deflagration-to-detonation transition in hydrogen/air mixtures with a concentration gradient, *Combust. Sci. Technol.* 184 (2012) 1903–1915.
- [16] K. Ishii, M. Kojima, Behavior of detonation propagation in mixtures with concentration gradients, *Shock Waves* 17 (2007) 95–102.
- [17] K. Iwata, Osamu Immura, Kazuhiro Akihama, Hiroshi Yamasaki, Shinji Nakaya, Mitsuhiro Tsue, Numerical study of self-sustained oblique detonation in a non-uniform mixture, *Proc. Combust. Inst.* 38 (2021) 3651–3659.
- [18] K. Iwata, S. Nakaya, M. Tsue, Numerical investigation of the effects of nonuniform premixing on shock-induced combustion, *AIAA J.* 54 (2016) 1682–1692.
- [19] K. Iwata, S. Nakaya, M. Tsue, Numerical simulation of incompletely premixed oblique detonation stabilized on a solid surface, *Trans. JSASS Technol.* 14 (2016) 31–38.
- [20] K. Iwata, S. Nakaya, M. Tsue, Wedge-stabilized oblique detonation in an inhomogeneous hydrogen-air mixture, *Proc. Combust. Inst.* 36 (2017) 2761–2769.
- [21] L.V. King, On the convection of heat from small cylinders in a stream of fluid: determination of the convection constants of small platinum wires with applications to hot-wire anemometry, *Phil. Trans. R. Soc. A* 214 (1972) 373–432.
- [22] M. Karasawa, N. Choji, M. Sekido, A contribution to evaluation method of diffusion coefficient, *J. Fiber Sci. Technol.* 28 (1972) 353–358.
- [23] M.S. Kuznetsov, V.I. Alekseev, S.B. Dorofeev, I.D. Matsukov, J.L. Boccio, Detonation propagation, decay, and reinitiation in nonuniform gaseous mixtures, *Symp. (Int.) Combust.* 27 (1998) 2241–2247.
- [24] K. McGrattan, S. Hostikka, R. McDermott, J. Floyd, C. Weinschenk, K. Overholt, Fire Dynamic Simulator, NIST Special Publication 1019, National Institute of Standards and Technology, Gaithersburg, Maryland, USA, 2016.
- [25] P. Wolanski, Detonative propulsion, *Proc. Combust. Inst.* 34 (2013) 125–158.
- [26] R.A. Gross, Oblique detonation waves, *AIAA J.* 1 (1963) 1225–1227.
- [27] R. Dunlap, R.L. Brehm, J.A. Nicholls, A preliminary study of the application of steady-state detonative combustion to a reaction engine, *Jet Propuls.* 28 (1958) 451–456.
- [28] S. Boulaï, P. Vidal, R. Zitoun, Experimental investigation of detonation quenching in non-uniform compositions, *Combust. Flame* 172 (2016) 222–233.
- [29] S. Gordon, B.J. McBride, Computer Program for Calculation of Complex Chemical Equilibrium Compositions and Applications, NASA Reference Publication 1311, NASA Lewis Research Center, Cleveland, Ohio, USA, 1996.
- [30] S. Maeda, J. Kasahara, A. Matsuo, Oblique detonation wave stability around a spherical projectile by a high time resolution optical observation, *Combust. Flame* 159 (2012) 887–896.
- [31] S. Maeda, S. Kanno, I. Yoshiki, T. Obara, *Sci. Technol. Energet. Mater.* 77 (2016) 79–85.
- [32] S. Maeda, S. Sumiya, J. Kasahara, A. Matsuo, Initiation and sustaining mechanisms of stabilized oblique detonation waves around projectiles, *Proc. Combust. Inst.* 34 (2013) 1973–1980.
- [33] S. Maeda, S. Sumiya, J. Kasahara, A. Matsuo, Scale effect of spherical projectiles for stabilization of oblique detonation waves, *Shock Waves* 25 (2015) 141–150.
- [34] V.V. Vlasenko, V.A. Sabel'nikov, Numerical simulation of inviscid flows with hydrogen combustion behind shock waves and in detonation waves, *Combust. Explos. Shock Waves* 31 (1995) 376–389.
- [35] Y. Daimon, A. Matsuo, Analogy between wedge-induced steady oblique detonation and one-dimensional piston-supported unsteady detonation, *Sci. Technol. Energetic Mater.* 65 (2004) 111–115.
- [36] Y. Fang, Z. Hu, H. Teng, Z. Jiang, H.D. Ng, Numerical study of inflow equivalence ratio inhomogeneity on oblique detonation formation in hydrogen-air mixtures, *Aerospace Sci. Technol.* 71 (2017) 256–263.